

Quantitative Study of Loess Microstructure At Micrometer Scale Via X-Ray Computed Tomography

Weina Yuan (✉ yuanwn@chd.edu.cn)

Chang'an University

Wen Fan

Chang'an University

Research Article

Keywords: Loess, X-ray computed tomography, Three-dimensional microstructure, Representative elementary volume, Two-dimensional microstructure

Posted Date: July 20th, 2021

DOI: <https://doi.org/10.21203/rs.3.rs-655352/v1>

License:   This work is licensed under a Creative Commons Attribution 4.0 International License. [Read Full License](#)

Abstract

The macroscopic properties of loess are significantly controlled by its microstructure. Quantitative analysis of loess microstructure is essential for modeling the microstructure and further incorporating the microstructural effects into geotechnical practice. However, loess has a multi-scale microstructure ranging from nanometer to millimeter scales, and researches at the particle resolution are still inadequate. This study systematically investigates the micrometer-scale microstructure of loess from Jingyang, China, via X-ray computed tomography and the image segmentation method that was explored for loess. The statistical analyses of three-dimensional (3D) microstructure reveal that the particle size follows the Weibull distribution, and the distributions of pore and pore throat sizes obey the gamma distribution. Most particles are blade-shaped, with a peak length ratio of (1.53–1.64):1.28:1. The particles are oriented in the polar directions but not azimuthally, in a spherical coordinate system, exhibiting a transversely isotropic structure. The quantitative microstructures of the loess and paleosol samples were slightly different irrespective of the large aggregates developed in paleosol sample. Moreover, the representative elementary volume obtained through porosity is also applicable for the analysis of microstructural parameters such as size distribution, shape factor, orientation angle, and pore connectivity. Besides, the two-dimensional (2D) distributions of the particle, pore, and pore throat sizes agree with the 3D distributions, except that the former were marginally smaller. However, the 2D sectional analysis of shape, arrangement, and pore connectivity cannot adequately represent the 3D characteristics.

Introduction

Loess is a type of Quaternary aeolian sediment with a loose and open metastable structure that is widely distributed in the middle latitudes (Pye 1995). Due to the special geotechnical properties of loess, especially those associated with water, geological hazards frequently occurred in loess region and loess has been classified as a problematic soil in engineering construction (Juang et al. 2019; Dijkstra et al. 1994). Researchers have long recognized the relationship between the microstructure and macroscopic properties of loess. Many have verified that the collapsibility, compression and shear behaviors of loess were significantly controlled by its microstructure (particle, pore and contact) (Xu et al. 2019; Wen and Yan 2014; Assallay et al. 1997). The influences of pore structure on soil permeability have been quantitatively addressed (Ren and Santamarina 2018). The microstructure evolution of loess induced by water, loading and landslide has also been studied (Wei et al. 2020; Zuo et al. 2019; Yuan et al. 2019). The characteristics of particles in loess are commonly utilized as indicators of the paleoclimatic environment (Sun et al. 2018). Therefore, knowledge regarding loess microstructure at the particle and pore scales is very crucial for understanding its geotechnical engineering properties and revealing the underlying geological hazards mechanisms. Particularly, a quantitative study will be essential for modeling the microstructure of loess and incorporating the microstructural effects into geotechnical practice.

Loess microstructure has been extensively studied using evolving experimental techniques. Laser particle analyzer and mercury intrusion porosimetry are routinely used to measure the particle and pore size distributions of loess, respectively (Li and Shao 2020; Sun et al. 2004). Microscopy-based observation methods, such as scanning electron microscopy and optical microscope, can provide visual information of the soil microstructure from natural or epoxy resin sections and are thus the most common tool for two-dimensional (2D) microstructure research. Numerous studies have adopted these methods to qualitatively investigate the microstructure of loess, including its particle, pore, and contact characteristics, and an increasing number of studies have quantitatively analyzed the loess microstructure in terms of size, shape, and arrangement, by combining these methods with image processing techniques (Deng et al. 2020; Giménez et al. 2012; Assallay 1998; Gao 1988). Recently researchers began to analyze the three-dimensional (3D) loess microstructure with the development of X-ray CT that can provide nondestructive testing (Li and Shao 2020; Yu et al. 2020; Wei et al. 2020; Li et al. 2019; Wei et al. 2019; Li et al. 2018). However, great efforts are still required, especially in the aspect of 3D quantitative study of loess microstructure.

Loess has a hierarchical microstructure with a high porosity. It developed both the pores associated with particles or aggregates and worm or plant root holes, with sizes up to the millimeter scale (Li and Shao 2020; Li et al. 2019). The size of aggregates in loess varies considerably in the micrometer scale, while the particles are generally smaller than 75 μm , and fine

composition in the nanometer scale is also common in various strata of the Chinese Loess Plateau (Sun 2006; Dijkstra et al. 1994). Consequently, the study of loess microstructure is a multi-scale problem ranging from nanometer to millimeter scales. A tradeoff exists between the observation resolution of the apparatus and the image field of view; a higher resolution leads to a smaller field of view. Therefore, it is difficult to obtain the full-scale microstructural characteristics of loess using only one apparatus or resolution. Comprehensive investigations of the loess microstructure at various scales are very necessary. However, most of the previous works on loess microstructure by CT were conducted at resolution of dozens of micrometers, which are insufficient to identify particles. Recently, a limited number of studies investigated the microstructure of loess at particle resolution by using X-ray micro-computed tomography (Yu et al. 2020; Wei et al. 2020; Wei et al. 2019). Nevertheless, a systematic analysis of the loess microstructure at the micrometer scale is still rare. Besides, the representative elementary volume or area (REV or REA), which is the minimum sample size and must be sufficiently large for the sample properties to be independent of the size, is vital for quantitative analysis. However, the REV or REA derived based on porosity may not be adequate for the analysis of microstructural parameters as discussed in the work of Al-Raoush and Papadopoulos (2010). Moreover, although the 3D loess microstructure has been investigated in a few studies, many quantitative analyses are generally performed using 2D observational techniques because of their affordability and convenience. Hence, the validity of the parameters obtained through 2D observation must be examined. These issues were also basic topics needed to be addressed in the quantitative research of loess microstructure.

In this paper, loess microstructure was investigated using an X-ray CT apparatus at resolution of 1 μ m in order to address the research gaps mentioned above. The full-scale microstructural characteristics of samples were firstly summarized based on experimental results. An image processing method suitable for the microstructure of loess was explored and utilized for further quantitative statistics. Then the particle and pore characteristics of samples were systematically analyzed from 3D view. The determination method of REV for the micrometer-scale microstructure was discussed, and the representativeness of 2D microstructural parameters for 3D characteristics was also examined. The results intend to improve the research of loess microstructure, especially in terms of the three-dimensional quantitative analysis, and also provide implications for the macroscopic behaviors.

Sample And Experiments

The samples for this study were collected from Jingyang, Shaanxi province, China. The strata in this zone consist of loess–paleosol sequences. Both loess and paleosol samples during the middle Pleistocene (Q₂) ages were obtained from two adjacent strata at depths of 20–22 m near the Zhaitoucun landslide site on the southern Jingyang platform. The bulk density was determined using an undisturbed sample with a diameter of 61.8 mm and height of 20 mm. Grain density was measured using the pycnometer method. The liquid limit and plastic limit were determined using a cone penetrometer. The mineral compositions were analyzed using X-ray powder diffraction. Table 1 lists the physical indices of the loess and paleosol samples. The bulk porosities, calculated using dry bulk density and grain density data, were approximately 43% and 42% for the loess and paleosol samples, respectively. The particle size distributions were measured using a laser particle analyzer (Fig. 1). The samples had a particle size of less than 75 μ m and a silt fraction (2–50 μ m) of 78–80%. Additionally, the loess sample contained 14% clay (< 2 μ m), while the paleosol sample contained 20% clay.

Table 1
Basic physical indices of samples.

Sample type	Dry bulk density (g/cm ³)	Grain density (g/cm ³)	Porosity (%)	Liquid limit (%)	Plastic limit (%)	Mineral composition (%)			
						Quartz + Feldspar	Calcium	Clay minerals	Others
Loess	1.55	2.7	43	33.7	16.8	53.1	13.3	26.6	7
Paleosol	1.58	2.71	42	32.2	15.7	55.7	6.4	35.6	2.3

Bulk samples were acquired after removing topsoil to avoid gathering plant root holes and wormholes. The top and bottom planes of the bulk samples were parallel to the bedding, which was essentially horizontal. The bulk samples were carefully cut into cylinders with a diameter and height of approximately 2 mm. The top and bottom planes of the cylindrical samples were also parallel to the bedding. The prepared samples were dried using the low-vacuum freeze-drying method before being used for the X-ray CT experiment. The samples were then scanned using a ZEISS Xradia 520 Versa 3D X-ray microscope with a spatial resolution of up to 700 nm. The samples were scanning at a spatial resolution of 1 μm at a voltage of 50 kV and a current of 81 μA . After scanning for 12 h, images with a diameter of 2,000 voxels and a height of 2,000 slices were obtained for each sample.

Image Processing Method

Image segmentation, which identifies individual particles and pores from CT images, is a prerequisite for quantitative analysis of microstructures. Various image segmentation algorithms have been developed and implemented in software such as Matlab, ImageJ, Mimics, or Avizo. Given the complexity of geomaterials, none of these algorithms could be applicable to images for all types of soils (Pal et al. 1993). Thus efforts were made to obtain good image processing results for the samples. Figure 2 presents the image processing workflow realized in Avizo.

The first step in image segmentation is the division of images into solid voxels (contacted particles) and pore voxels (connected pores). A media filter was used to reduce the noise of the images before segmentation. In principle, a CT image is a map of the attenuation coefficients of the X-rays passing through a sample (Taina et al. 2008). Owing to the strong contrast of X-ray attenuation between the pore space and the soil solid, the particles and pores can be easily separated through the commonly used threshold segmentation method. The global intensity threshold value for the images of each sample was determined by comparing the segmented porosity with the corresponding porosity in Table 1. Voxels with intensity values higher and lower than the global threshold were identified as contacted particles and connected pores, respectively.

The second step of image segmentation involves separating the contacted particles and connected pores into individual particles and pores. The watershed algorithm is widely utilized to obtain individual particles and pores for soils, and its theory is described in many literatures (Baychev et al. 2019; Zheng and Hryciw 2016). The pores were segmented using the watershed algorithm based on Beucher and Meyer (1993). We attempted to segment the particles solely using this algorithm. However, since loess has a wide range of particle sizes, the result was not satisfactory. The following image processing method was explored to separate the contacted particles (Fig. 2). As depicted in Fig. 3, the particles in the samples exhibited a range of intensities, this is because different minerals cause different X-ray attenuations. Thus, light particles with high intensities were extracted first from the contacted particles via threshold segmentation, and this extraction was helpful in segmenting the remaining dark particles. Then, the extracted light particles and remaining dark particles were segmented. The former were scattered and could be easily separated into individual particles, however, the separation of the latter was laborious. For the separation of the latter, the hierarchical watershed algorithm was used. Subsequently the edges of separated dark particles were detected using the Laplacian zero-crossing algorithm and were then subtracted from the images with the residual edges being eliminated through erosion and dilation. Finally, the separated dark and light particles were merged for quantitative analysis (Fig. 3).

The image segmentation results were satisfactory as illustrated in Fig. 3. The particle-size distributions obtained from the segmented images were compared with those obtained from the laser particle analyzer (Fig. 4). Only particles larger than 1 μm were counted, considering the image resolution. Figure 4 shows that the particles from the image analysis are marginally smaller than those from the laser particle analyzer. This was ascribed to the difference between the two methods. The image analysis separated the particles and measured them according to their geometric morphologies. The laser particle analyzer measured the particles based on the principle of light scattering and the coherent particles were isolated using a $(\text{NaPO}_3)_6$ dispersant before the test. The particles that retained their geometric integrity may be separated after being dissolved in deionized water in the presence of the dispersant. Thus the comparison results were reasonable (Fig. 4).

After segmenting the images, we obtained the individual particles and pores and analyzed the quantitative microstructural parameters defined in Tables 2 and 3. The porosity, equivalent diameter, shape factor, and orientation angle can be directly measured using Avizo. However, calculation of pore throat, coordinate number and tortuosity requires topological information of the pores. The pore network model (PNM) developed by Sochi (2010), in which the pore structure is a network of pores connected by throats, was used to determine pore throat and pore coordinate number. The pore structure of the samples was simplified into a tree-like structure, and the centerlines of the structure were extracted using Avizo to obtain tortuosity.

Table 2
Interpretations of 3D microstructural parameters.

Parameter	Symbol	Definition	Explanation
Equivalent diameter	EqD	$EqD = (6 V_{3D} / \pi)^{(1/3)}$	V_{3D} represents the volume of an individual particle or pore.
Shape factor	L_1, L_2, L_3		L_1 is the maximum Feret diameter. L_2 is the largest distance between two parallel lines touching the particle boundary and lying in a plane orthogonal to L_1 . L_3 is the largest segment touching the particle boundary at its end points and lying in a plane orthogonal to both L_1 and L_2 .
Orientation angle	φ, θ		φ and θ are the orientation angles of the maximum Feret diameter direction of particle or pore in 3D spherical coordinate system.
Porosity	n	$n = V_v / V_t$	V_v and V_t represent the pore volume and the total volume of the samples, respectively.
Pore throat equivalent diameter	EqL	$EqL = (4A / \pi)^{(1/2)}$	A is the contact area between two connected pores. It is the narrowest region between pores.
Pore coordinate number	CN		CN represents the number of branches connected with a pore.
Tortuosity	τ	$\tau = l_c / l_d$	l_c and l_d are the curved length and linear distance between start and end point of the centerlines in the pore.

Table 3 Interpretations of 2D microstructural parameters.

Parameter	Symbol	Definition	Explanation
Equivalent diameter	EqD_{2D}	$EqD_{2D} = (4 Area / \pi)^{(1/2)}$	$Area$ is the area of an individual particle or pore.
Orientation angle	θ_{2D}		θ_{2D} is the orientation angle of the direction of the maximum Feret diameter in a 2D polar coordinate system.
Porosity	n_{2D}	$n_{2D} = A_v / A_t$	A_v and A_t represent the pore area and total area of the samples, respectively, in 2D space.
Pore throat equivalent diameter	EqL_{2D}	$EqL_{2D} = l$	The narrowest region between two pores in 2D space is a line segment, and the length of line segment (l) is EqL_{2D} .
Pore coordinate number	CN_{2D}		CN_{2D} represents the number of branches connected with a pore in 2D space.
Tortuosity	τ_{2D}	$\tau_{2D} = l_{c2D} / l_{d2D}$	l_{c2D} and l_{d2D} are the curved length and linear distance between the start and end point of the centerlines in the pore.

Results And Discussions

4.1 General

Figure 5 presents examples of typical CT slices from the samples. As observed in Fig. 5(a), skeletons of the loess sample were mainly composed of uniformly distributed coarse particles. As shown in Fig. 5(f), large aggregates comprising both coarse particles and fine clays were scarce in the loess sample. Most of the pores in the loess sample were inter-particle pores (Fig. 5(d)) and overhead pores, which are large pores formed by lots of particles and are prone to collapse under loading or water (Fig. 5(e)). Compared with the loess sample, the paleosol sample had a considerably denser microstructure (Figs. 5(b) and 5(c)), which agrees with the larger bulk density and higher clay fraction of the paleosol sample (Table 1). Fewer overhead pores were present in this sample, and the inter-particle pores were smaller (Fig. 5(g)). However, densely packed aggregates, which flocked together, were observed in this sample, along with large inter-aggregate pores (Figs. 5(c) and 5(h)).

The REV for the quantitative analysis of aggregates (30–220 μm) and inter-aggregate pores (15–200 μm) observed in the paleosol sample would be beyond the micrometer scale. Thus these aggregates were not considered in this study. This issue can be addressed by selecting larger samples and lower resolutions. In addition, the studied samples generally exhibited a bimodal distribution, with boundary values of approximately 1–2 μm for coarse to fine components, as indicated by the particle size distributions in Fig. 1. The resolution of 1 μm was insufficient for analyzing the fine components. Hence the coarse components, which were the major constituent of samples, were the focus of this study.

Size, shape, and arrangement are the fundamental elements of soil microstructure (Assallay, 1998). The parameters of equivalent diameter, shape factor, and orientation angle, as explained in Tables 2 and 3, were used to represent the three aforementioned elements. Pore connectivity is a critical property of the pore structure, especially in the analysis of hydraulic behavior, and was represented by the pore throat equivalent diameter, coordinate number, and tortuosity (Tables 2 and 3). Thus, in this study, the quantitative characteristics of particles (equivalent diameter, shape factor, and orientation angle) and pores (porosity, equivalent diameter, orientation angle, pore throat equivalent diameter, pore coordinate number and tortuosity) were statistically investigated. The distributions of these parameters were also quantified using common probability distribution functions. The goodness of fit was estimated using the adjusted R-square value (Eq. (1)), which can be less than or equal to 1; a value closer to 1 indicates a better fit.

$$R - square = 1 - \frac{(n - 1) \sum_{i=1}^n (y_i - \hat{y}_i)^2}{(n - m) \sum_{i=1}^n (y_i - \bar{y})^2} \quad (1)$$

where y_i represents the statistical data, \bar{y} the mean value, and \hat{y}_i the fitting values. n is the number of statistical data and m the number of fitted coefficients in the function.

4.2 Representative elementary volume

Selection of the REV is the first step in quantitative analysis of microstructures. In this study, the REV was obtained based on porosity. The porosity was calculated from the CT images using the traditional cube method, as shown in Fig. 6(a). First, an initial point, at a random location in the samples, was taken as the starting point of a cube with a side of 100 μm . Then, the cube was enlarged equally in the three dimensions with fixed initial point. For each initial point, a group of cubes with sides of 100–1,000 μm in increments of 100 μm was extracted. The porosities for the groups were calculated and are presented in Figs. 6(b) and 6(c). The porosities of the smaller cubes exhibited large fluctuations, and the fluctuation decreased as the cube size increased. The porosity remained stable as the side length of the cubes increased up to 700–800 μm . Thus, the preferred REV was 800 $\mu\text{m} \times 800 \mu\text{m} \times 800 \mu\text{m}$.

The stationary porosity of the loess sample in Fig. 6(b) is 39–42%, while that of the paleosol samples in Fig. 6(c) is 32–35%. For the loess sample, the stationary porosity agreed with the calculated bulk porosity of 43% (Table 1). This was attributed to

the homogeneous structure of the loess sample, as shown in Fig. 5(a). However, the paleosol sample exhibited a significantly lower stationary porosity than its calculated bulk porosity of 42% (Table 1). The large inter-aggregate pores of the paleosol sample were eliminated in the quantitative analysis of the images, as discussed in Sect. 4.1. The bulk porosity was calculated based on the bulk density, accordingly, a sample with size of a diameter of 61.8 mm and height of 20 mm was examined, wherein the presence of inter-aggregate pores were unavoidable. Consequently, it is reasonable that the stationary porosity of the paleosol sample was smaller than the calculated bulk porosity. Furthermore, the comparison between the stationary porosity of 32–35% and the calculated bulk porosity of 43% indicated that most of the pore volume in the paleosol sample was contributed by the inter-particle and overhead pores.

To determine whether the REV obtained from the porosity was suitable for the other parameters listed in Table 2, each parameter was evaluated on several cubes. The cubes all had the same dimensions of 800 μm \times 800 μm \times 800 μm , and were randomly located in the samples. The discreteness of the parameters caused by different cubes was estimated in terms of the standard deviation and was expressed as an error bar. As it was difficult to define the volume of pore connectivity, frequency percentages for the pore connectivity parameters were counted by number (Figs. 7–11), while those for the other parameters were counted by volume (Fig. 12). The statistical results of eight parameters with the error bar—the particle equivalent diameter (Fig. 7), particle shape factor (Figs. 8(a) and 8(b)), particle orientation angle (Fig. 9(b)), pore equivalent diameter (Fig. 10), pore orientation angle (Fig. 11(a)), pore throat equivalent diameter (Fig. 12(a)), pore coordinate number (Fig. 12(b)) and tortuosity (Fig. 12(c))—showed that all parameters fluctuated within a narrow range. This phenomenon was consistent with the result of porosity at the stable stage (Figs. 6(b) and 6(c)). The fluctuations of these parameters may have been caused by the natural heterogeneity of the soil, which was unavoidable. However, these fluctuations had no impact on the overall distribution of the parameters for the loess and paleosol samples, as shown in Figs. 7–12. Thus, the REV obtained from the porosity was also appropriate for the analysis of other microstructural parameters listed in Table 2.

4.3 Quantitative characterization of 3D microstructure

The quantitative particle characteristics in terms of size, shape, and arrangement and the pore structure characteristics in terms of pore size, pore arrangement, and pore connectivity were discussed in the following subsections.

4.3.1 Particle characteristics

According to Fig. 7, the 3D particle size (EqD) was generally smaller than 70 μm . The mean values for the loess particles and paleosol particles were 27.2 μm and 21.7 μm , respectively. The side size of the REV was approximately more than 10 times the maximum particle size and 25–30 times the mean value. The fitting results in Fig. 7 show that particle sizes of all samples obeyed the Weibull distribution. Eq. (2) describes the probability density function. This distribution function was also demonstrated to be suitable for loess samples from seven sections across the Chinese Loess Plateau by Sun et al. (2004) and for 160 loess samples by Zhao et al. (2013).

$$f(x) = \frac{\alpha}{\beta^\alpha} x^{\alpha-1} \exp(-(x/\beta)^\alpha) \quad (2)$$

where α and β are the function coefficients of the Weibull distribution.

Characterizing the particle morphology is a complex task. Many descriptors of particle morphology have been proposed in previous literatures (Howarth 2010; Blott and Pye 2008; Rogers and Smalley 1993), however, it is difficult to find one that describes particle morphology comprehensively. Generally, particle morphology involves two aspects, shape and surface texture (Blott and Pye 2008). This work mainly focuses on the basic shape of particles. A combination of three dimensions, L_1 , L_2 and L_3 (Table 2), was utilized to describe the 3D particle shape. The data of these dimensions were reduced to 2D data using the ratios of L_2/L_1 and L_3/L_2 ; the corresponding volume percentage distributions are shown in Figs. 8(a) and 8(b). The data (L_2/L_1 , L_3/L_2 , volume percentage) were fitted efficiently using the probability density function of a bivariate normal distribution (Eq. (3)). The volume percentage peaks in Figs. 8(a) and 8(b) for the loess and paleosol samples represent shape ratios of approximately 1.53:1.28:1 ($L_1:L_2:L_3$) and 1.64:1.28:1 ($L_1:L_2:L_3$), respectively. These statistical values were different

from the result (8:5:2) obtained by Rogers and Smalley (1993), who used the random number theory. Four shape categories were defined according to the modified Zingg classification (Howarth 2010; Rogers and Smalley 1993)—disk ($L_1 = L_2 > L_3$), sphere ($L_1 = L_2 = L_3$), blade ($L_1 > L_2 > L_3$), and rod ($L_1 = L_2 < L_3$). A statistical result with an accuracy of 10% for calculation is presented in Fig. 8(c). The result shows that 56–57% of the particles were shaped like blades, 16–19% like rods, 5–6% like disks, and 17–21% like spheres.

$$f(x, y) = \frac{1}{2\pi\sigma_1\sigma_2\sqrt{1-\rho^2}} \exp\left(\frac{-1}{2(1-\rho^2)} \left(\frac{(x-\mu_1)^2}{\sigma_1^2} - 2\rho\frac{(x-\mu_1)(y-\mu_2)}{\sigma_1\sigma_2} + \frac{(y-\mu_2)^2}{\sigma_2^2}\right)\right) \quad (3)$$

where μ_1 , μ_2 , σ_1 , σ_2 , and ρ are the function coefficients of the bivariate normal distribution.

Particle arrangement was expressed as the distribution of the maximum Feret diameter orientations, which were displayed as the polar angle ($0^\circ \leq \varphi \leq 90^\circ$) and azimuthal angle ($-180^\circ \leq \theta \leq 180^\circ$) in a spherical coordinate system where the Z axis was perpendicular to the bedding (Fig. 9(a)). The orientation angles (φ , θ) in the upper hemisphere of the spherical coordinate system were divided evenly into 31 groups. These groups were expressed by 31 markers, as shown in Fig. 9 (a) and 9(c). Figure 9(c) showed the top-down view of Fig. 9(a) along the Z axis. The volume percentages for the 31 groups shown in Fig. 9 (b) are also expressed as the size of the markers in Fig. 9(c), i.e., a group with a bigger marker had a larger volume percentage. The preferred orientation can be clearly observed in Fig. 9(c). Groups with large markers all had φ values between 60° and 90° , but their θ values were random. The observations revealed that particles in the samples were oriented in the polar directions but not azimuthally, implying a transversely isotropic structure. This result is consistent with the fact that loess, a type of aeolian soil, has a sedimentary structure (Xu et al. 2019; Heller and Liu 1982). The anisotropy index (I_a) expressed in Eq. (4) is generally used to reflect the overall anisotropy of soil arrangement (Li et al. 2020; Tovey and Krinsley 1992). An increase in I_a from 0 to 100% represents a change in microstructure from random or isotropic to preferred aligned or completely anisotropic. The I_a of the analyzed particles was 74–76%, which indicated that they were generally preferred aligned. Figure 9(d) shows that I_a decreased as the particle size increased, which means that smaller particles are prone to being preferred oriented; specifically, particles smaller than $5 \mu\text{m}$ had an I_a of up to 96–98%.

$$I_a = (d_{\max} - d_{\min})/d_{\max} \times 100\% \quad (4)$$

where d_{\max} and d_{\min} are the largest and smallest volume percentages among those of all 31 groups of 3D orientation angles.

4.3.2 Pore structure characteristics

Figure 10 presents the 3D pore size distributions of the samples. The mean *EqDs* of pores for the loess and paleosol samples were $20.9 \mu\text{m}$ and $13.9 \mu\text{m}$, respectively. The fitting results show that the pore sizes of all samples obeyed the gamma distribution (Eq. (5)):

$$f(x) = \frac{1}{b^a \int_0^\infty t^{a-1} \exp(-t) dt} x^{a-1} \exp(-x/b) \quad (5)$$

where a and b are the function coefficients of the gamma distribution.

The analysis method for 3D pore arrangement was the same as that for particle arrangement. The volume percentages for the 31 groups of orientation angles shown in Fig. 11(a) are expressed using 31 markers with different sizes in a spherical coordinate system from a top-down view (Fig. 11(b)). The statistical results in Fig. 11(b) show that pores were generally randomly arranged. The I_a value of 47–48% also indicated that the pore direction was slightly isotropic. This implied that the anisotropy of inter-particle pores was not dependent on that of particles.

The pore throat sizes of the samples also obeyed the gamma distribution, as shown in Fig. 12(a). The mean values of pore throat size for the loess and paleosol samples were $4.8 \mu\text{m}$ and $3.3 \mu\text{m}$, respectively. The pores and pore throats of the loess sample were all larger than those of the paleosol sample. Figures 12(b) and 12(c) show that the distributions of pore coordinate number (CN) and tortuosity (τ) were irregular and therefore cannot be described statistically. The average CN was

5.5–5.8, indicating that most of the pores were connected to approximately five other pores or pore throats. The average τ was 1.213–1.216. The paleosol sample had a smaller CN but a larger τ than the loess sample did. In previous works on Chinese loess that used X-ray CT, the macropores of samples from Jingyang, Shaanxi province had an average CN of 2.56 and an average τ of 1.12 at a resolution of 73.9 μm (Li et al. 2019), and those from Yuci, Shanxi province had an average CN of 3.15 at a resolution of 60 μm (Li et al. 2018). The aforementioned average CN and average τ values were smaller than those of the pores in the samples used in this study, the majority of which were inter-particle and overhead pores at a resolution of 1 μm , with large inter-aggregate pores eliminated. This suggested these inter-particle and overhead pores had a denser, more complex pore structure than the macropores.

4.4 Differences between 2D and 3D microstructures

Various sections of the 2D microstructure from different directions were quantitatively analyzed, as shown in Fig. 13(a). These sections were extracted after segmenting the 3D microstructure, to negate the differences induced by the image processing method. S3 was the section along the horizontal bedding direction. S1, S2, S3, and S4 had different dip angles with respect to the horizontal bedding and an angular spacing of 45° each. S1, S5, S6, and S7 were along the vertical direction and had an angular spacing of 45° each. Non-overlapping sections, all parallel to S3 and with a size of 3,000 $\mu\text{m} \times 3,000 \mu\text{m}$, were extracted randomly from different locations in the samples. The porosity values calculated from these sections was shown in Figs. 6(b) and 6(c). According to the results, the porosity values exhibited negligible discreteness, and thus, the size was within the REA for the 2D calculation. Since an elongated particle in 2D space can be rod-like or flaked in 3D space, the results with the 2D shape obtained from the sections cannot represent the overall 3D shape of particle. Therefore, only the 2D parameters from Table 3 were measured in the sections with a size of 3,000 $\mu\text{m} \times 3,000 \mu\text{m}$. The statistical results were summarized in Figs. 13–15.

4.4.1 Size

Figs. 13 (b)–(d) show the distributions of 2D size for the particles, pores and pore throats. The particle size distribution from all the sections could be well described using the Weibull function for the loess and paleosol samples with mean EqD_{2D} values of 22.7–23.2 μm and 17.5–17.7 μm , respectively. The differences between the sections were small. Both the pore sizes and pore-throat sizes from all sections obeyed the gamma distribution. The results of the statistical analysis are presented in Table 4. The mean sizes of the pore and pore throat of the loess sample were 17.8–18.3 μm and 5.0–5.2 μm , and those of the paleosol samples were 11.2–11.4 μm and 3.4–3.6 μm . The values of these parameters from different sections also exhibited minor differences. By comparison, it was verified that the 2D size distributions of the particles, pores and pore throats agreed with the corresponding 3D results, except that the mean values of the 2D size were smaller than those of the 3D size.

Table 4
Results of statistical analysis for size distributions of particles, pores and pore throats.

Sample type	Particle size				Pore size				Pore throat size				
	Weibull distribution				Gamma distribution				Gamma distribution				
	Mean	<i>R-square</i>	<i>a</i>	β	Mean	<i>R-square</i>	<i>a</i>	<i>b</i>	Mean	<i>R-square</i>	<i>a</i>	<i>b</i>	
Loess sample	3D	27.19	0.9970	2.29	33.29	20.88	0.9956	5.98	3.82	4.76	0.9809	3.45	1.50
	S1	23.09	0.9948	2.01	28.43	18.03	0.9927	4.64	4.32	4.99	0.9935	1.76	2.98
	S2	23.04	0.9952	2.03	28.33	18.02	0.9924	4.73	4.23	5.22	0.9943	1.66	3.32
	S3	23.19	0.9940	2.01	28.33	18.17	0.9934	4.70	4.26	4.98	0.9953	1.85	2.83
	S4	22.84	0.9955	2.05	27.93	18.11	0.9931	4.64	4.31	5.22	0.9934	1.68	3.27
	S5	23.12	0.9945	2.00	28.26	17.91	0.9926	4.66	4.25	5.16	0.9943	1.71	3.16
	S6	23.02	0.9954	2.06	28.22	18.30	0.9928	4.62	4.36	5.00	0.9949	1.79	2.90
	S7	22.73	0.9934	2.02	27.54	17.84	0.9925	4.71	4.18	5.24	0.9946	1.70	3.24
Paleosol sample	3D	21.66	0.9958	2.35	27.02	13.94	0.9862	5.10	2.83	3.27	0.9752	4.72	0.84
	S1	17.49	0.9959	2.10	21.83	11.27	0.9808	5.36	2.17	3.42	0.9980	2.12	1.75
	S2	17.64	0.9942	2.06	21.89	11.31	0.9817	5.27	2.22	3.53	0.9985	2.12	1.79
	S3	17.65	0.9942	2.08	21.96	11.15	0.9803	5.34	2.18	3.44	0.9983	2.16	1.72
	S4	17.62	0.9947	2.07	21.97	11.21	0.9834	5.32	2.20	3.57	0.9989	2.11	1.81
	S5	17.61	0.9937	2.08	21.88	11.16	0.9840	5.35	2.17	3.53	0.9986	2.12	1.80
	S6	17.56	0.9945	2.06	21.96	11.20	0.9784	5.30	2.20	3.42	0.9979	2.16	1.71
	S7	17.51	0.9945	2.07	21.99	11.37	0.9816	5.23	2.25	3.63	0.9983	2.09	1.86

4.4.2 Arrangement

Fig. 14 summarizes the statistical results of 2D arrangement obtained from the seven sections. The orientations of the maximum Feret diameters for the 2D particles and pores were presented as a rose diagram in the polar coordinate system, where the orientation angle θ_{2D} (0–180°) was divided into 10 groups, and the volume percentage for each group was represented by the polar radius (Figs. 14(a) and (b)). According to the statistical results, the particles tended to be preferred oriented, and different sections had different orientation distributions (Fig. 14(a)). The calculated I_a for particles from different sections varied from 53.1 to 79.4%, with the horizontal section (S3) having the smallest value (Fig. 14(c)). In addition, Fig. 14(b) shows that the pore orientation was generally random and that pores in all sections had consistent orientation distributions. The I_a of the pores differed only slightly among the sections, albeit much more than the corresponding 3D values did (Fig. 14(d)). These results demonstrated that sectional analysis cannot represent the 3D preferred orientation or anisotropy.

4.4.3 Pore connectivity

Fig. 15 presents the results of the average pore coordinate number and average tortuosity in both 2D and 3D space. The results showed that the paleosol sample had a smaller pore coordinate number and larger tortuosity than the loess sample did. The values were all slightly different in different sections. For all sections, the average CN_{2D} and average τ_{2D} were 2.4–2.8 and 1.231–1.271, respectively. The average CN_{2D} was much smaller than the corresponding 3D value (5.5–5.9), whereas

the average τ_{2D} was larger than the 3D value (1.213–1.216). These differences between the 2D and 3D values can be explained by the pore structure characteristics. In the 3D space, the pores were connected to several other pores via long and narrow channels, as shown in Fig. 3. However, the 2D parameters were calculated considering the connected pores only in the 2D section. Consequently, the 3D tortuous and complex channels outside the section may have been omitted from the calculation. Therefore, CN_{2D} was much smaller while τ_{2D} much larger than the respective 3D values.

4.5 Implications for macroscopic behaviors

The instability of loess engineering and occurrence of geological hazards (such as landslides) can be easily caused by the failure of the contact zone between the loess and paleosol strata owing to their differences in geotechnical properties, particularly their hydraulic behavior (Dijkstra et al. 2015; Lei 2014). The microstructure of loess is different from that of paleosol in terms of particles and pores, as clearly depicted in Fig. 5 and revealed by the results in Sect. 4. This is the primary cause for the differences in their geotechnical properties. Hydraulic behavior is mainly determined by the pore structure of soil. The results indicated that the paleosol sample possesses a considerably denser microstructure, smaller pores, and smaller pore throats than those of the loess sample. This explains why the permeability coefficient of paleosol is smaller than that of loess, despite that their porosity values are close. In addition, the porosity of paleosol is mainly due to the inter-particle and overhead pores, whereas the inter-aggregate pores are significantly large as discussed in Sect. 4.2. Thus the contributions of both types of pores to permeability cannot be neglected. However, the two types of pores should be studied at two different scales considering their size difference, and the results can then be integrated in the quantitative analysis of permeability and be used in further stability predictions.

Besides, the X-ray CT images revealed that the paleosol sample developed aggregates (30–220 μm). The properties of these aggregates when subjected to loading and watering, as well as the contributions of the aggregates to the strength of loess and stability of loess engineering, may be different from those of the particles. However, these issues are rarely considered in the existing literatures and should be addressed in future work.

Conclusions

The study revealed the multi-scale characteristics of loess microstructure, and focused on the micrometer-scale microstructure of loess, and also discussed the basic issues in the quantitative analysis of microstructure based on an investigation on the microstructures of loess and paleosol samples obtained from Jingyang in China via X-ray CT. The main conclusions are as follows.

The aggregates and inter-aggregate pores identified from the CT images, as well as the fine component identified by a laser particle analyzer exceeded the micrometer scale. They can be studied at the millimeter and nanometer scales, respectively, in future works. This study mainly investigated the microstructure of loess at the micrometer scale. The quantitative microstructural characteristics of loess were analyzed via image processing method explored for loess and accomplished in Avizo software. The results suggested that contacted particles of samples could be separated by combining a threshold segmentation step with watershed-based algorithm. The threshold segmentation step distinguished the contacted particles as light and dark ones according to their intensity difference and was quite helpful for improving the separation effects.

Based on porosity statistics, an REV of 800 $\mu\text{m} \times 800 \mu\text{m} \times 800 \mu\text{m}$ was selected for quantitative analysis of the 3D microstructure. The side length of the REV was approximately more than 10 times the maximum particle size and 25–30 times the mean value. The REV was also suitable for the analysis of microstructural parameters (equivalent diameter, shape factor, orientation angle, pore coordinate number and tortuosity) and their distributions. However, quantitative analysis should be conducted with multiple REV cubes to consider the slight fluctuations in parameters due to the natural heterogeneity of soil.

The statistical results of the 3D microstructural analysis showed that the particle sizes of the samples obeyed the Weibull distribution, with a mean value of 21.7–27.2 μm . Approximately 56–57% of the particles were shaped like blades with peak

length ratios ($L_1:L_2:L_3$) of 1.53:1.28:1 and 1.64:1.28:1 for the loess and paleosol samples, respectively. The particles were oriented in the polar directions but not azimuthally in a spherical coordinate system, indicating a transversely isotropic structure. The sizes of the pores and pore throats obeyed the gamma distribution. In general, the pores had a random arrangement. The average CN and τ of the pores in this study were larger than those of macropores of samples analyzed in previous studies. This suggests that the inter-particle and overhead pores had a more complex structure.

A comparative analysis of the 3D and 2D microstructural parameters showed that all the probability distribution functions for the size distributions of the particles, pores, and pore throats in the 2D space agreed with those in the 3D space, except when the mean 2D sizes were marginally smaller than the mean 3D sizes. The preferred orientation or anisotropy results obtained from single 2D sections cannot represent the characteristics of particles or the pore arrangement. The average CN_{2D} was much smaller than the respective 3D value, while the average τ_{2D} was larger than its 3D counterpart; therefore, a 3D analysis is pivotal for pore-connectivity analysis. These findings can serve as references for microstructure studies on other types of geomaterials.

Declarations

Acknowledgements

This work was supported by the National Natural Science Foundation of China [grant numbers 41807238 and 41630634].

References

1. Al-Raoush R, Papadopoulos A (2010) Representative elementary volume analysis of porous media using x-ray computed tomography. *Powder Technol* 200(1–2):69–77
2. Assallay AM, Rogers CDF, Smalley IJ (1997) Formation and collapse of metastable particle packings and open structures in loess deposits. *Eng Geol* 48(1–2):101–115
3. Assallay AM (1998) Structure and hydrocollapse behaviour of loess. Dissertation, Loughborough University
4. Baychev TG, Jivkov AP, Rabbani A, Raeini AQ, Xiong QR, Lowe T, Withers PJ (2019) Reliability of algorithms interpreting topological and geometric properties of porous media for pore network modelling. *Transp Porous Media* 128(1):271–301
5. Beucher S, Meyer F (1993) The morphological approach to segmentation: the watershed transformation. In: Dougherty ER (ed) *Mathematical morphology in image processing*. Marcel Dekker Inc, New York, pp 433–481
6. Blott SJ, Pye K (2008) Particle shape: a review and new methods of characterization and classification. *Sedimentology* 55(1):31–63
7. Deng LS, Fan W, Liu SP, Chang YP, Dai Y, Li YB (2020) Quantitative Research and Characterization of the Loess Microstructure in the Bai Lu Tableland, Shaanxi Province, China. *Adv Civ Eng* 3681382
8. Dijkstra TA, Rogers CDF, Smalley IJ, Derbyshire E, Li YJ, Meng XM (1994) The loess of north-central China: geotechnical properties and their relation to slope stability. *Eng Geol* 36:153–171
9. Gao GR (1988) Formation and development of the structure of collapsing loess in China. *Eng Geol* 25(2–4):235–245
10. Giménez RG, de la Villa RV, Martín JAG (2012) Characterization of loess in Central Spain: a microstructural study. *Environ Earth Sci* 65:2125–2137
11. Heller F, Liu TS (1982) Magnetostratigraphical dating of loess deposits in China. *Nature* 300:431–433
12. Howarth JJ (2010) The shape of loess particles reviewed. *Open Geosci* 2(1):41–44
13. Juang CH, Dijkstra TA, Wasowski J, Meng XM (2019) Loess geohazards research in China: advances and challenges for mega engineering projects. *Eng Geol* 251:1–10

14. Lei XY (2014) *The Cause of Formation, Prevention and Cure of Geological Disasters of Loess*. Peking University Press, Beijing
15. Li P, Shao SJ (2020) Can X-ray computed tomography (CT) be used to determine the pore-size distribution of intact loess? *Environ Earth Sci* 79(1):1–12
16. Li X, Lu YD, Zhang XZ, Fan W, Lu YC, Pan WS (2019) Quantification of macropores of Malan loess and the hydraulic significance on slope stability by X-ray computed tomography. *Environ Earth Sci* 78(16):522
17. Li XA, Hong B, Wang L, Li LC, Sun JQ (2020) Microanisotropy and preferred orientation of grains and aggregates (POGA) of the Malan loess in Yan'an, China: a profile study. *B Eng Geol Environ* 79:1893–1907
18. Li YR, He SD, Deng XH, Xu YX (2018) Characterization of macropore structure of Malan loess in NW China based on 3D pipe models constructed by using computed tomography technology. *J Asian Earth Sci* 154:271–279
19. Pal NR, Pal SK (1993) A review on image segmentation techniques. *Pattern recogn* 26(9):1277–1294
20. Pye K (1995) The nature, origin and accumulation of loess. *Quat Sci Rev* 14(7):653–667
21. Ren XW, Santamarina JC (2018) The hydraulic conductivity of sediments: A pore size perspective. *Eng Geol* 233:48–54
22. Rogers CDF, Smalley IJ (1993) The shape of loess particles. *Naturwissenschaften* 80(10):461–462
23. Sochi T (2010) Pore-scale modeling of Non-Newtonian flow in porous media. Dissertation, Imperial College London
24. Sun DH (2006) Super-fine grain size components in Chinese loess and their palaeoclimatic implication. *Quat Sci* 26(6):928–936 (in Chinese)
25. Sun DH, Bloemendal J, Rea DK, An ZS, Vandenberghe J, Lu HY, Su RX, Liu TS (2004) Bimodal grain-size distribution of Chinese loess, and its palaeoclimatic implications. *Catena* 55(3):325–340
26. Sun ZX, Jiang YY, Wang QB, Owens PR (2018) A fractal evaluation of particle size distributions in an eolian loess-paleosol sequence and the linkage with pedogenesis. *Catena* 165:80–91
27. Taina IA, Heck RJ, Elliot TR (2008) Application of X-ray computed tomography to soil science: A literature review. *Can J Soil Sci* 88(1):1–19
28. Tovey NK, Krinsley DH (1992) Mapping of the orientation of fine-grained minerals in soils and sediments. *Bull Int Assoc Eng Geol* 46:93–101
29. Wei TT, Fan W, Yuan WN, Wei YN, Yu B (2019) Three-dimensional pore network characterization of loess and paleosol stratigraphy from South Jingyang Plateau, China. *Environ Earth Sci* 78(11):333
30. Wei YN, Fan W, Yu B, Deng LS, Wei TT (2020) Characterization and evolution of three-dimensional microstructure of Malan loess. *Catena* 192:104585
31. Wen BP, Yan YJ (2014) Influence of structure on shear characteristics of the unsaturated loess in Lanzhou, China. *Eng Geol* 168:46–58
32. Xu L, Gao YC, Wei X (2019) Anisotropic behaviour of a saturated clayey loess. *Geothch Lett* 9(1):28–34
33. Yuan WN, Fan W, Jiang CC, Peng XL (2019) Experimental study on the shear behavior of loess and paleosol based on ring shear tests. *Eng Geol* 250:11–20
34. Yu B, Fan W, Fan JH, Dijkstra TA, Wei YN, Wei TT (2020) X-ray micro-computed tomography (μ -CT) for 3D characterization of particle kinematics representing water-induced loess micro-fabric collapse. *Eng Geol* 279:105895
35. Zhao P, Shao MA, Omran W, She DL (2013) A modified model for estimating the full description of soil particle size distribution. *Can J Soil Sci* 93(1):65–72
36. Zheng JX, Hryciw RD (2016) Segmentation of contacting soil particles in images by modified watershed analysis. *Comput Geotech* 73:142–152
37. Zuo L, Lourenco SDN, Baudet BA (2019) Experimental insight into the particle morphology changes associated with landslide movement. *Landslides* 16:787–798

Figures

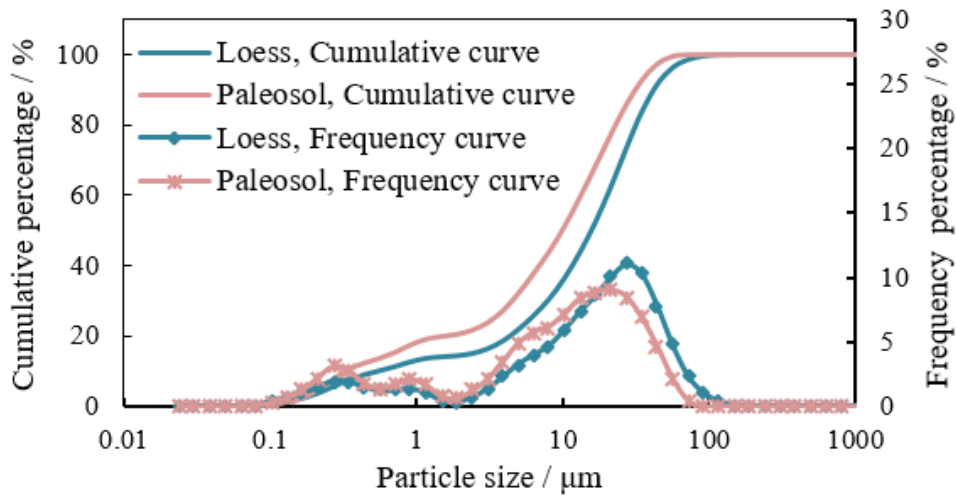


Figure 1

Particle size distribution.

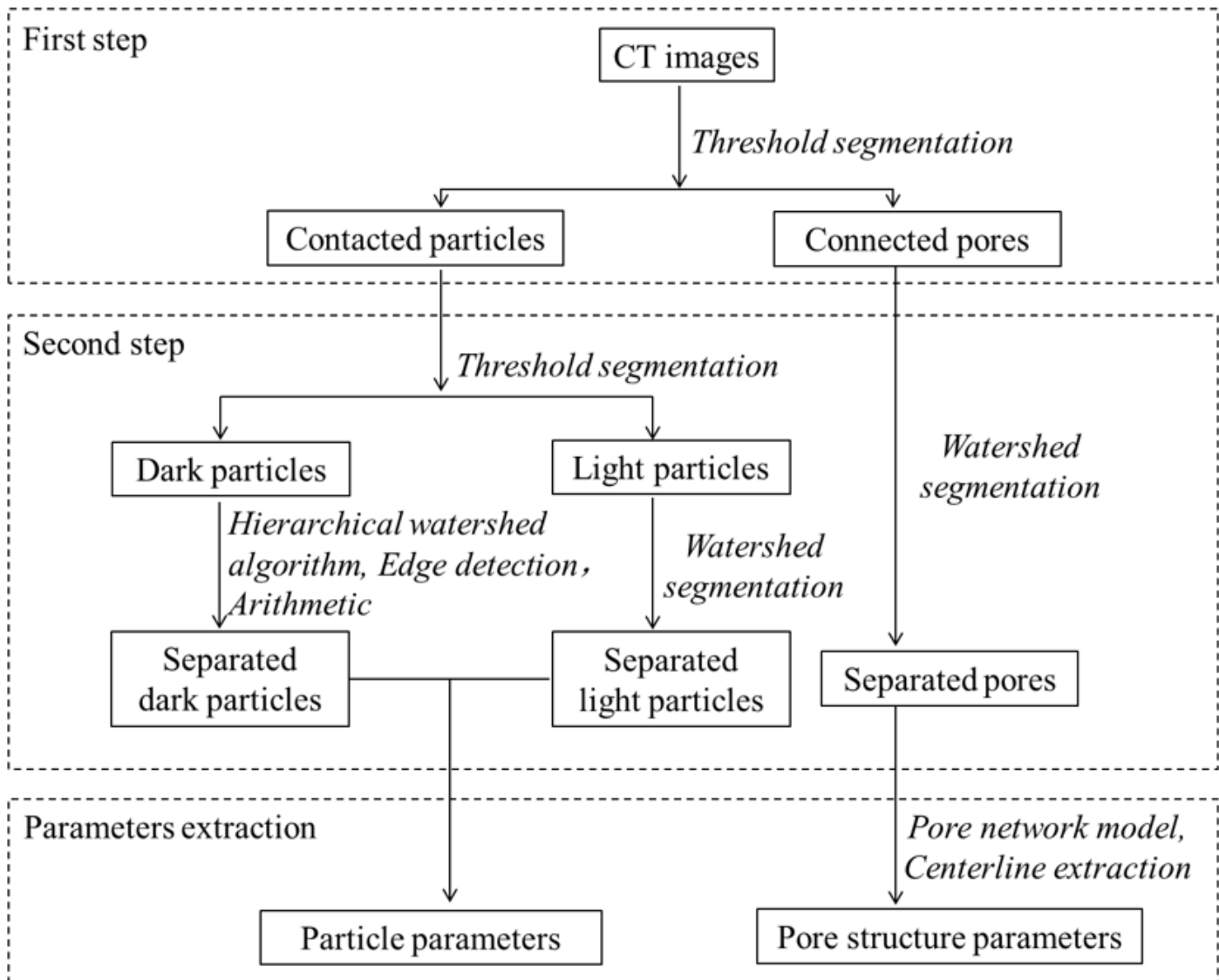


Figure 2

Image processing workflow.

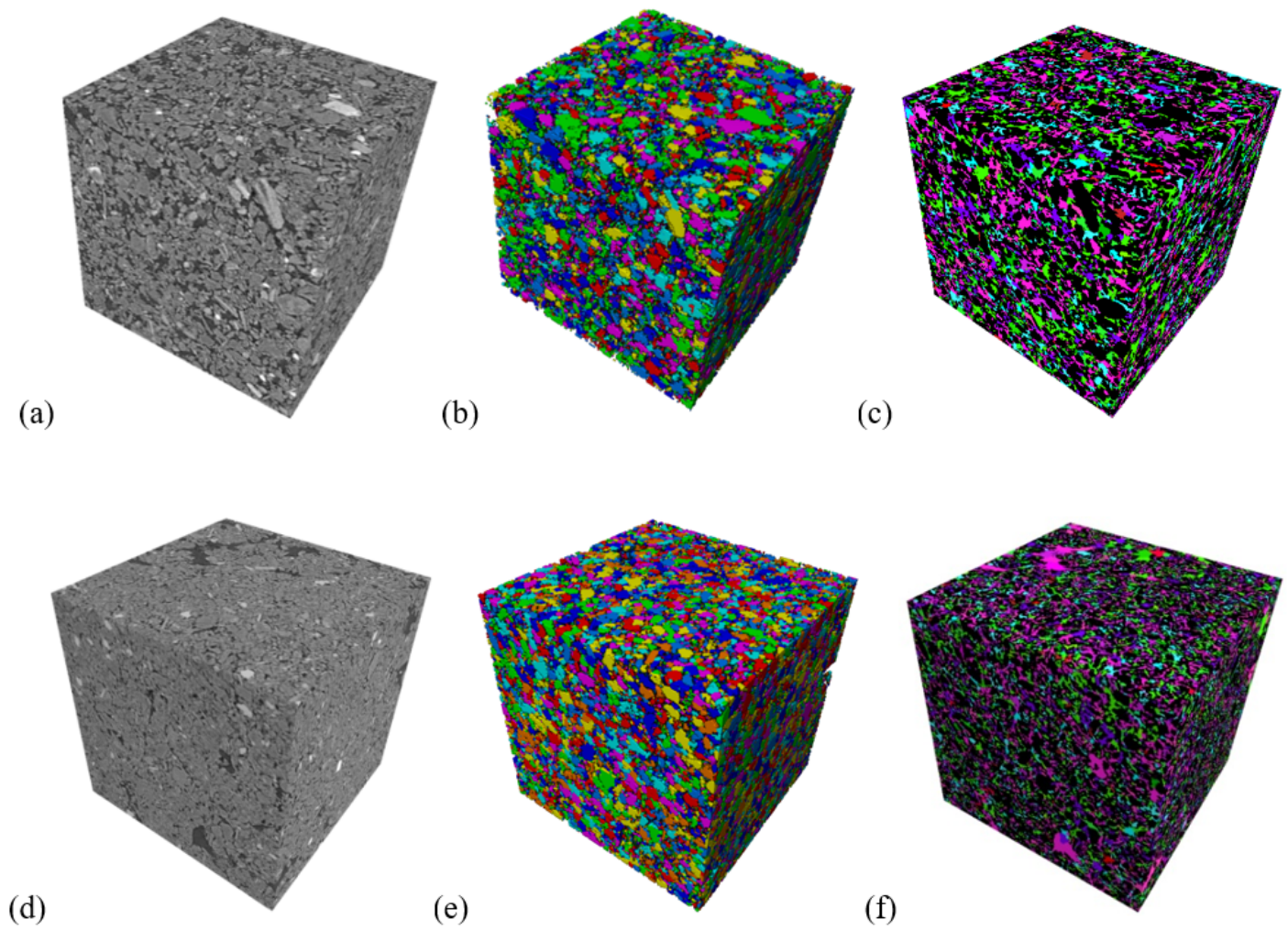


Figure 3

Image processing results with dimensions of $600 \mu\text{m} \times 600 \mu\text{m} \times 600 \mu\text{m}$. The segregated particles and pores were labeled with different colors. (a) CT images of loess sample; (b) Segmented loess particles; (c) Segmented loess pores; (d) CT images of paleosol sample; (e) Segmented paleosol particles; and (f) Segmented paleosol pores.

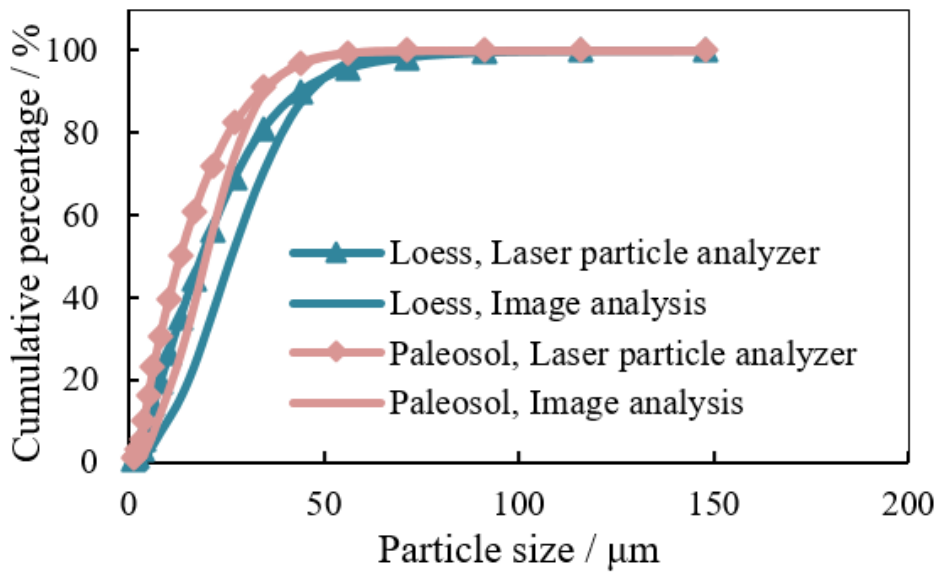


Figure 4

Comparison of results from laser particle analyzer and image analysis.

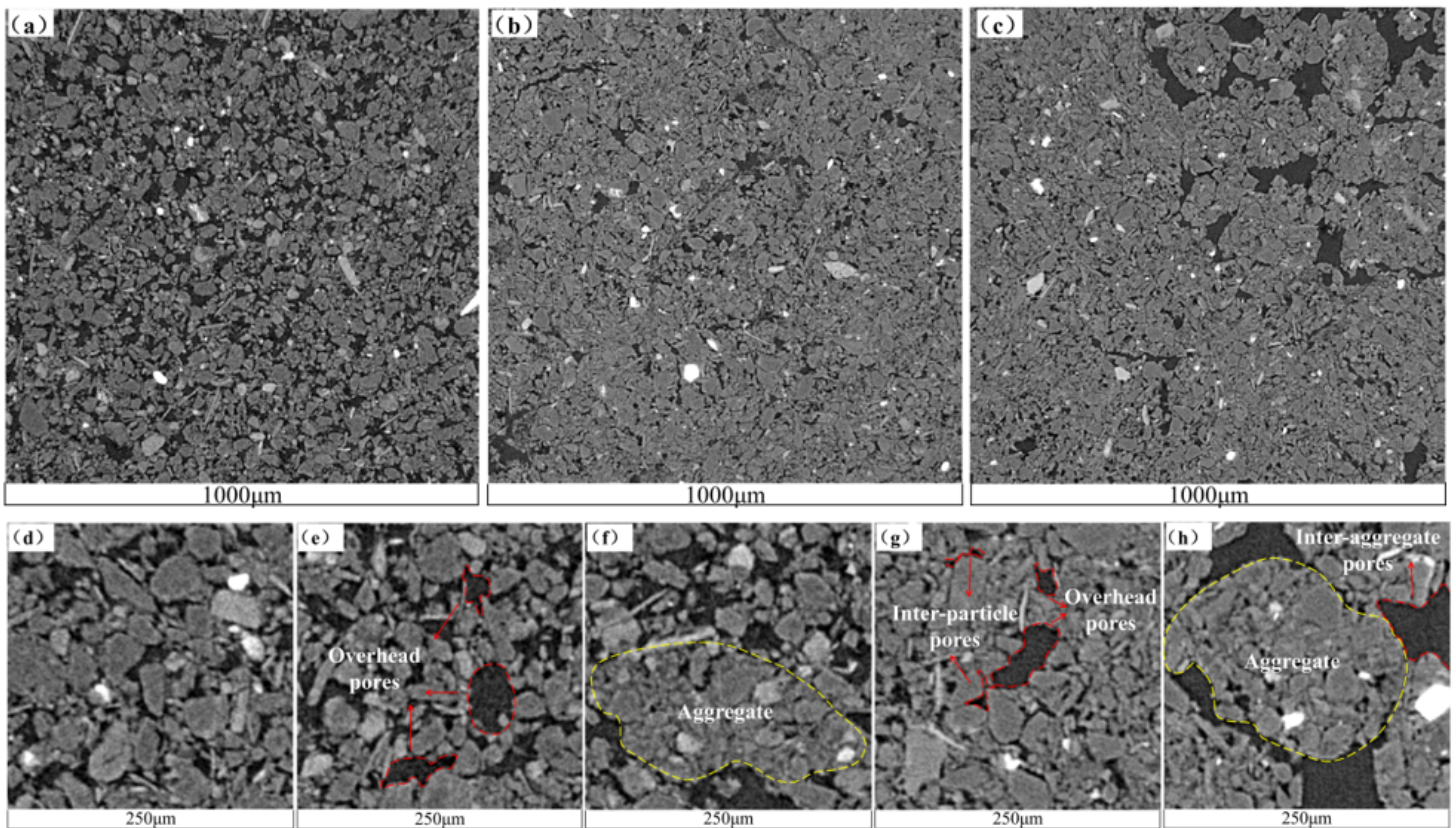


Figure 5

CT slices. (a) Loess sample, 1,000 micrometer by 1,000 micrometer; (b)–(c) Paleosol sample, 1,000 micrometer by 1,000 micrometer; (d)–(f) Loess sample, 250 micrometer by 250 micrometer; and (g)–(h) Paleosol sample, 250 micrometer by 250 micrometer.

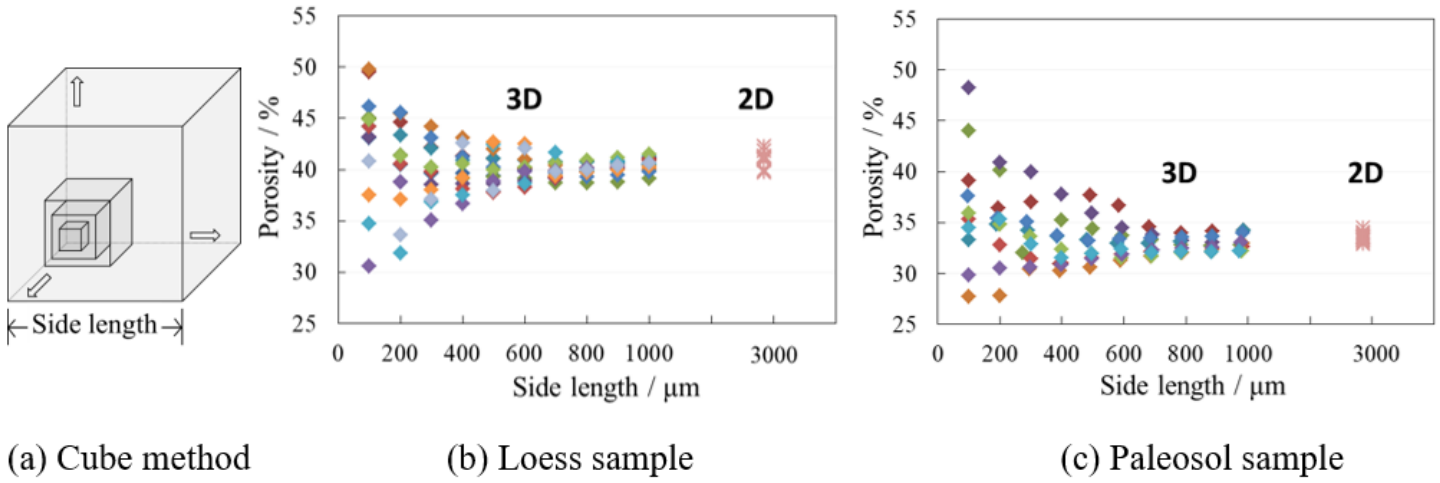


Figure 6

Porosity calculation for REV. For the 3D porosity results, points with the same color represent data from the same cube group with the same initial point as shown in Fig. 6(a). The 2D porosity results are calculated with a size of 3,000 $\mu\text{m} \times 3,000 \mu\text{m}$.

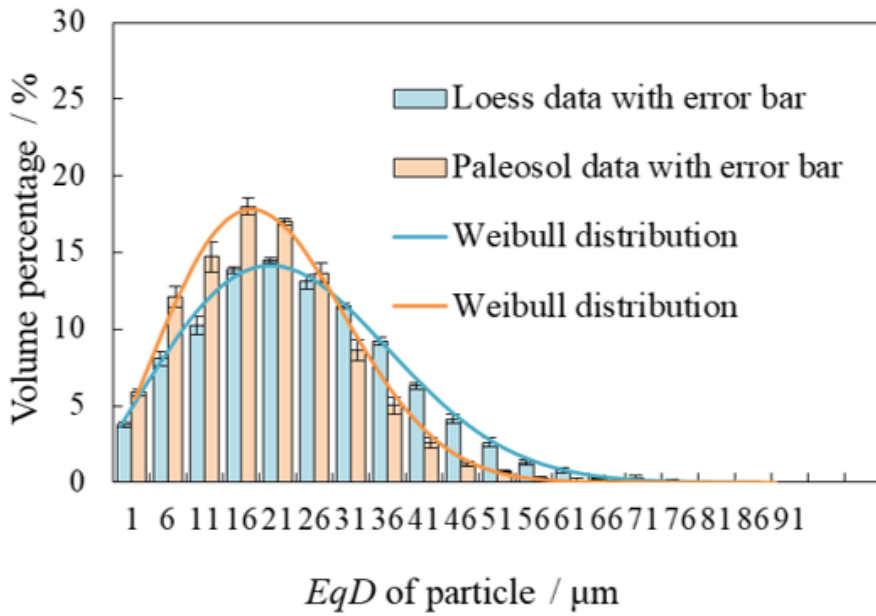
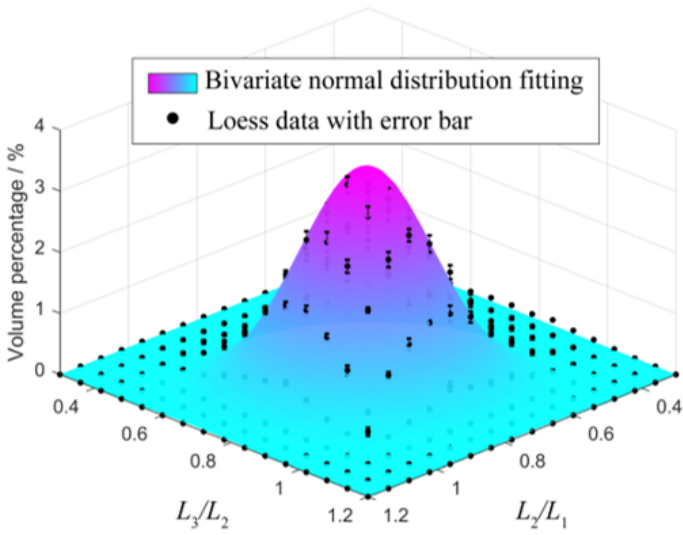
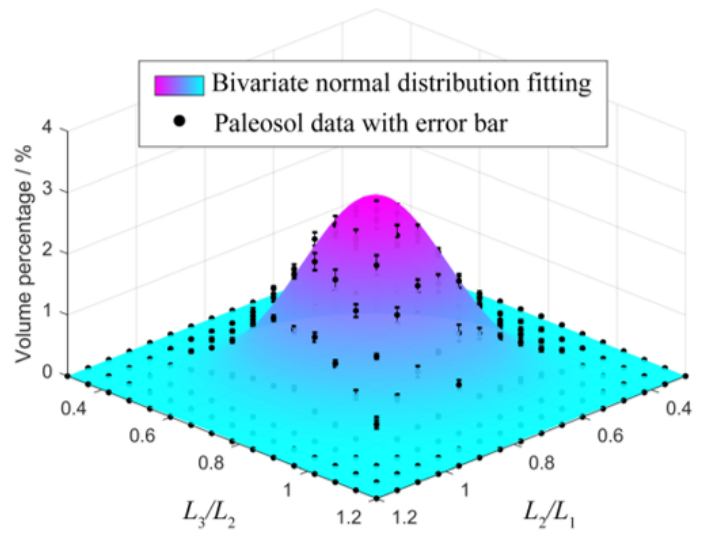


Figure 7

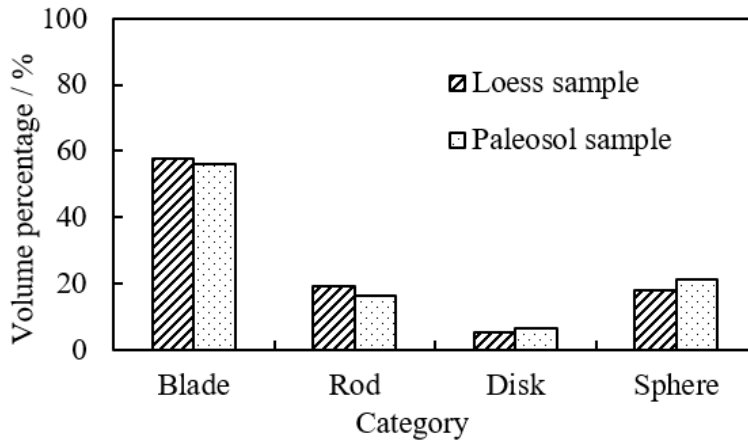
3D particle size distribution



(a) Particle shape distribution of loess sample



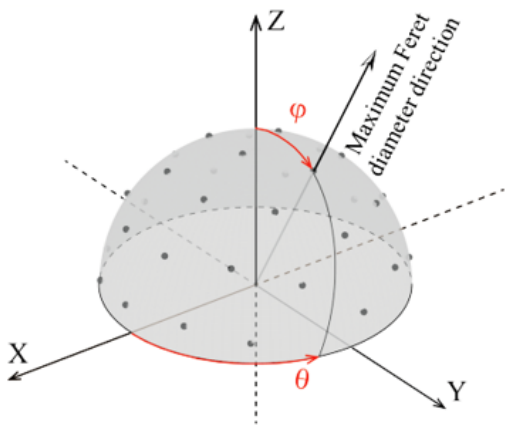
(b) Particle shape distribution of paleosol sample



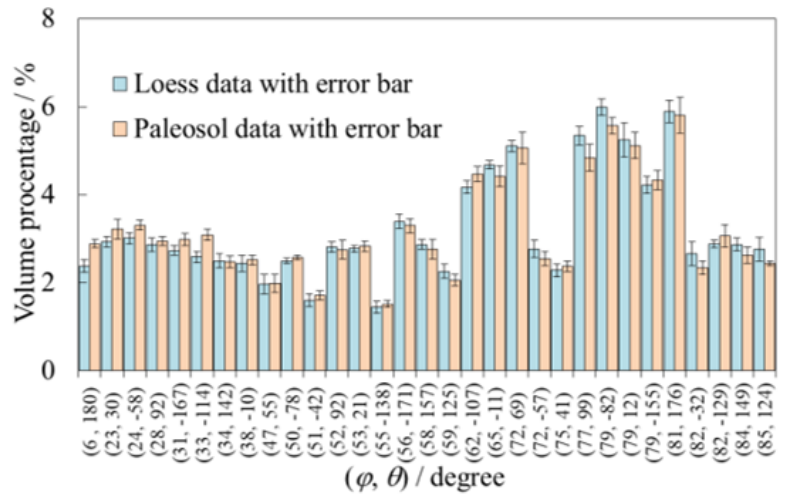
(c) Particle shape classification

Figure 8

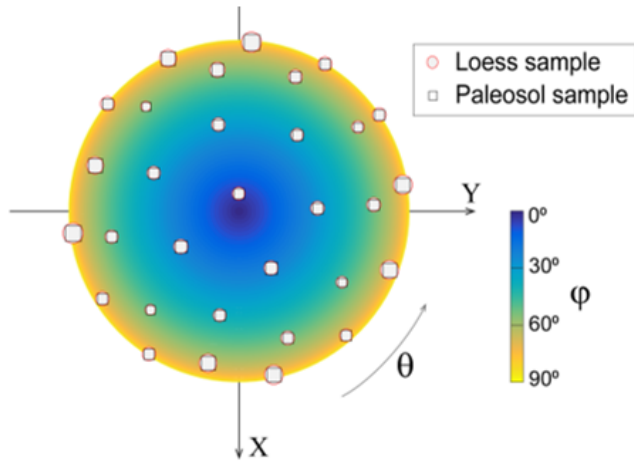
3D particle shape results



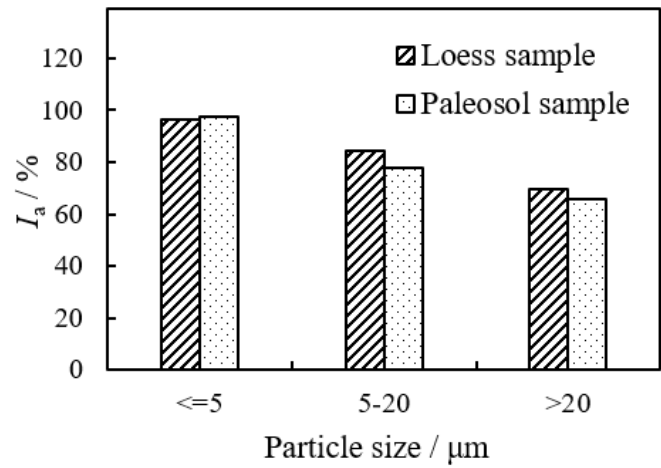
(a) Explanation of orientation angle



(b) Orientation angle distribution of particles



(c) Top-down view of particle arrangement



(d) Anisotropy index at different particle sizes

Figure 9

3D particle arrangement results. The orientation angle (φ, θ) was divided into 31 groups and expressed using the 31 markers in (a)–(c).

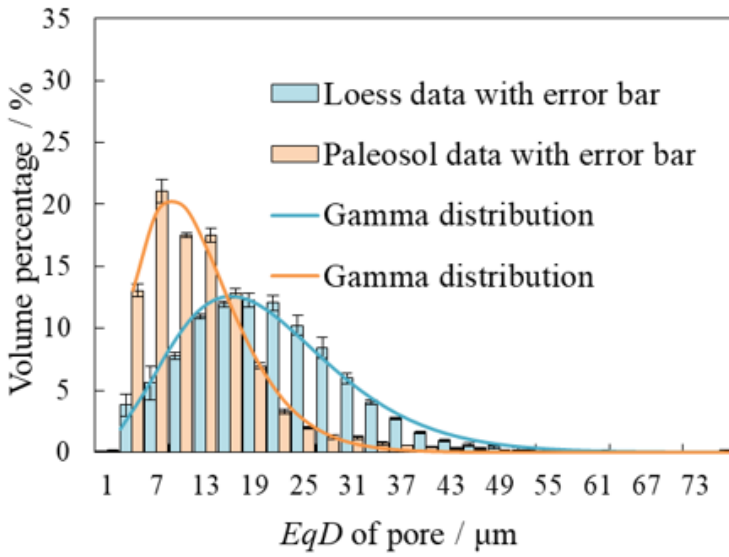
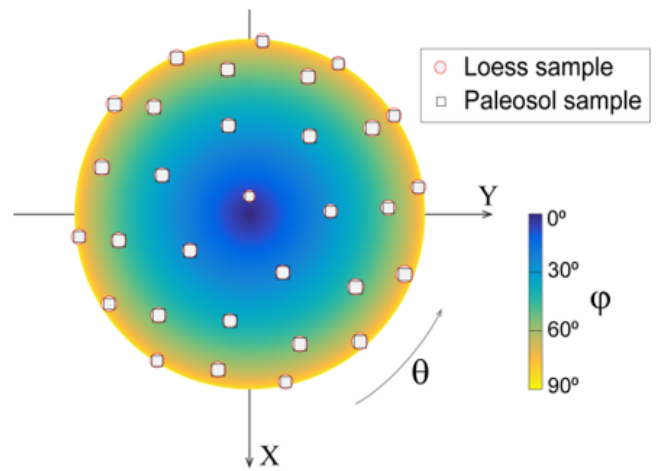
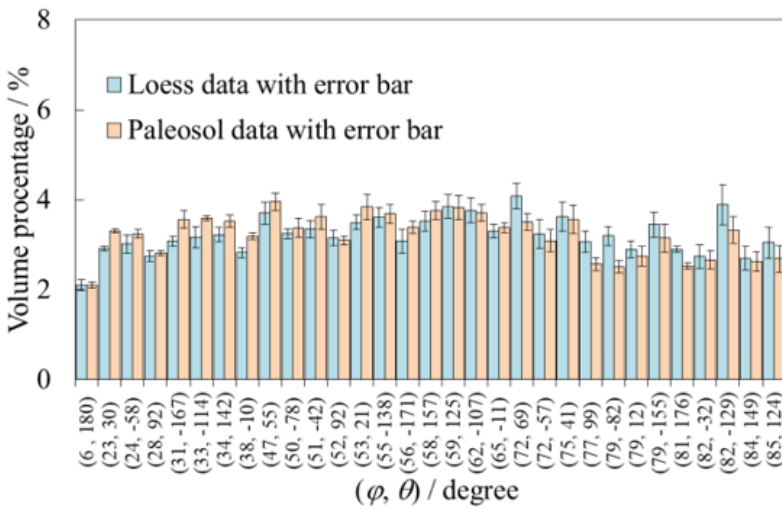


Figure 10

3D Pore size distribution



(a) Orientation angle distribution of pores

(b) Top-down view of pore arrangement

Figure 11

3D pore arrangement results

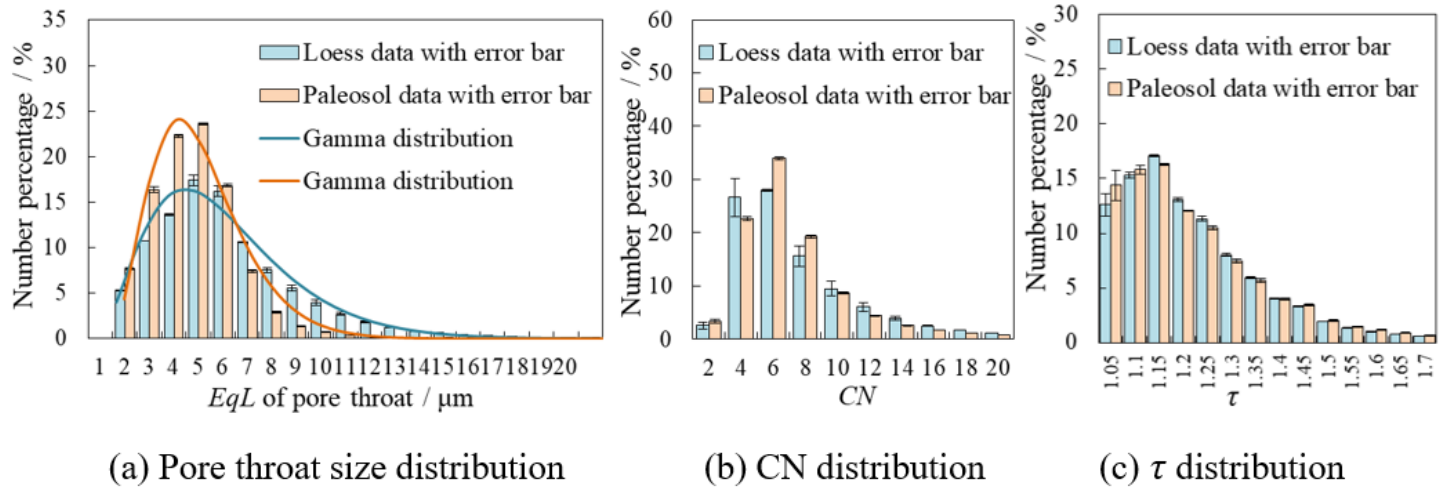
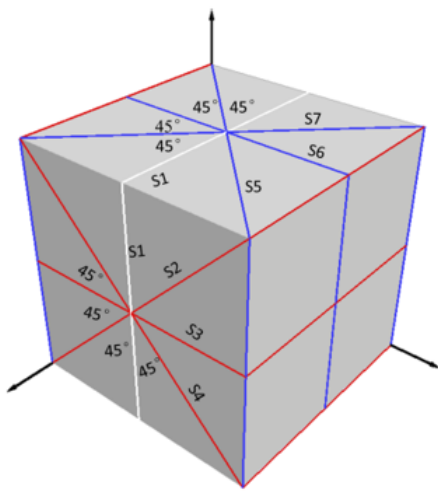
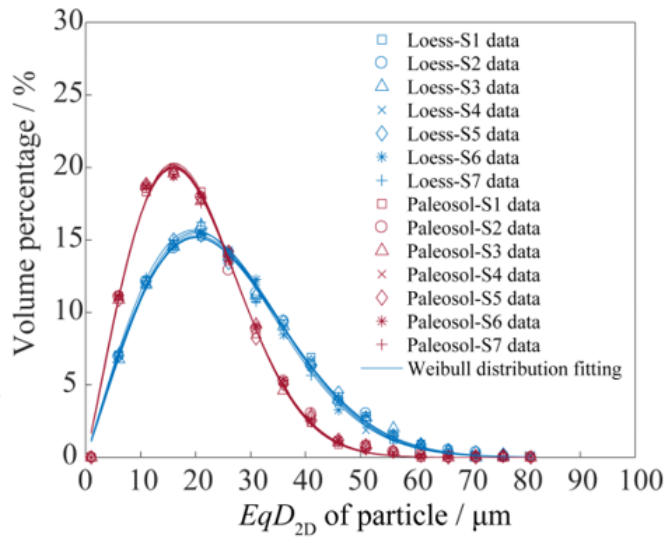


Figure 12

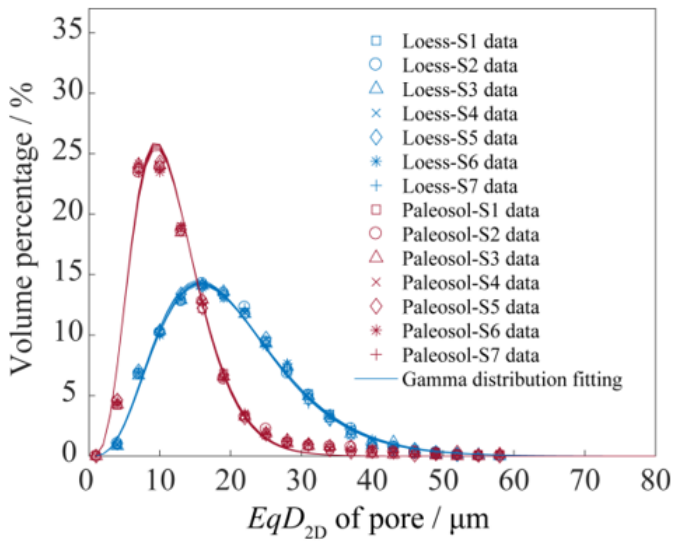
Statistical results of 3D pore connectivity parameters



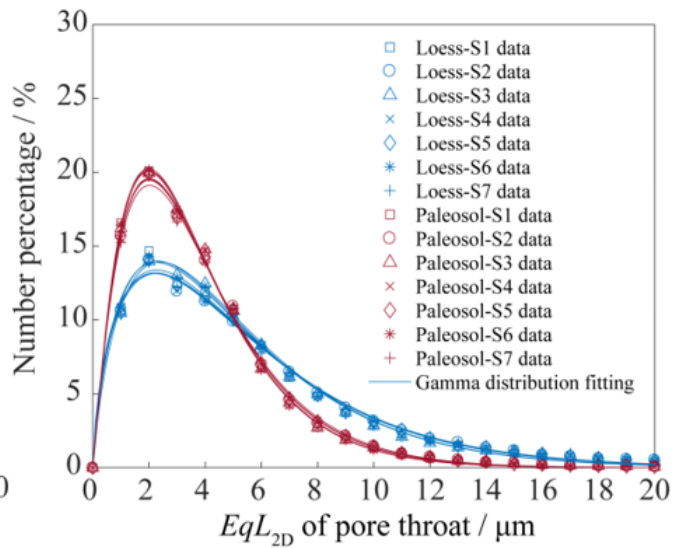
(a) Directions of sections



(b) 2D particle size distribution



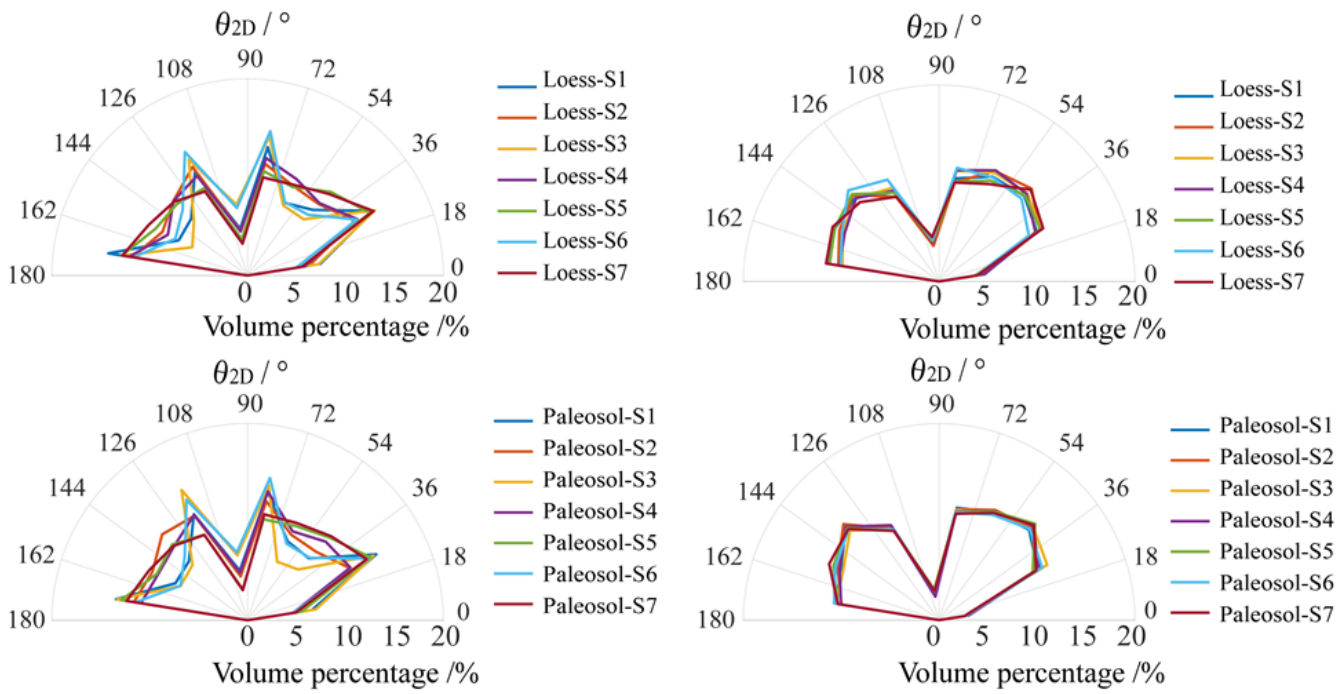
(c) 2D pore size distribution



(d) 2D pore throat size distribution

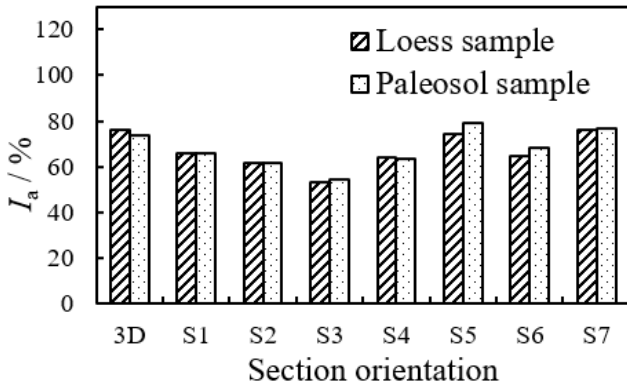
Figure 13

Statistical results of 2D size from various sections

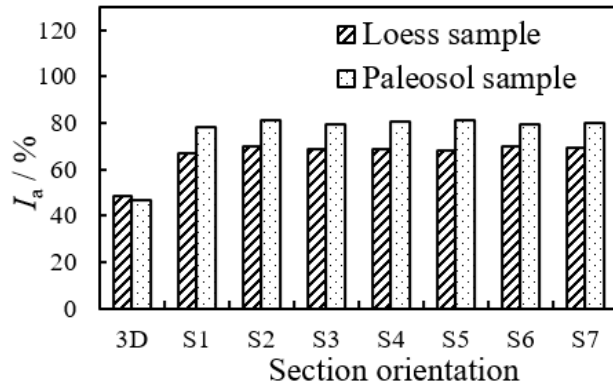


(a) Orientation angle distribution of particles

(b) Orientation angle distribution of pores



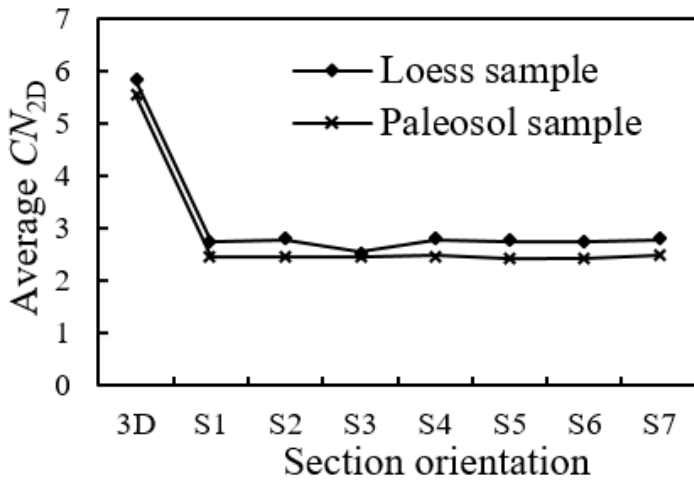
(c) Comparison of particle anisotropy



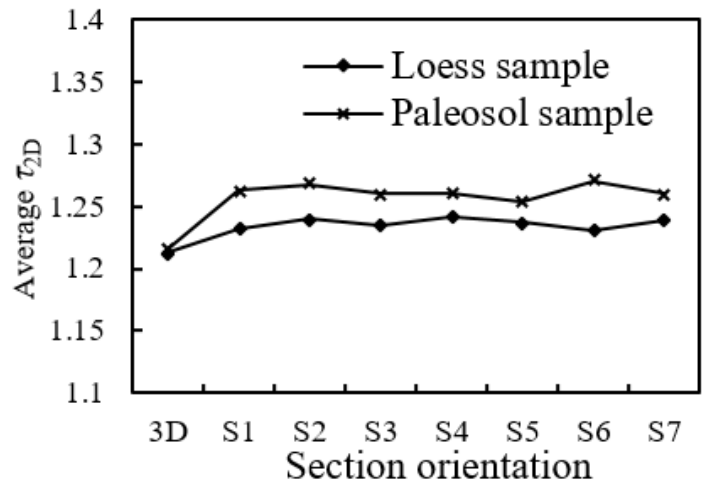
(d) Comparison of pore anisotropy

Figure 14

Statistical results of 2D arrangement



(a) Pore coordinate number



(b) Pore tortuosity

Figure 15

Comparison of 2D pore connectivity parameters